ADVANCED FUNCTIONAL MATERIALS
www.afm-journal.de

Materials Views
www.MaterialsViews.com

# Origin of Phonon Glass–Electron Crystal Behavior in Thermoelectric Layered Cobaltate

*Lijun Wu, Qingping Meng, Christian Jooss, Jin-Cheng Zheng, H. Inada, Dong Su, Qiang Li, and Yimei Zhu**

**Measurement of local disorder and lattice vibrations is of great importance for understanding the mechanisms whereby thermoelectric materials efficiently convert heat to electricity. Attaining high thermoelectric power requires minimizing thermal conductivity while keeping electric conductivity high. This situation is achievable by enhancing phonon scattering through specific structural disorder (phonon glass) that also retains sufficient electron mobility (electron crystal). It is demonstrated that the quantitative acquisition of multiple annular-dark-field images via scanning transmission electron microscopy at different scattering-angles simultaneously allows not only the separation but also the accurate determination of static and thermal atomic displacements in crystals. Applying the unique method to the layered thermoelectric material $(Ca_2CoO_3)_{0.62}CoO_2$ discloses the presence of large incommensurate displacive modulation and enhanced local vibration of atoms, largely confined within its $Ca_2CoO_3$ sublayers. Relating the refined disorder to ab initio calculations of scattering rates is a tremendous challenge. Based on an approximate calculation of scattering rates, it is suggested that this well-defined deterministic disorder engenders static displacement-induced scattering and vibrational-induced resonance scattering of phonons as the origin of the phonon glass. Concurrently, the crystalline $CoO_2$ sublayers provide pathways for highly conducting electrons and large thermal voltages.**

## 1. Introduction

The efficiency of conversion of heat to electric power in solid-state thermoelectric generators is governed by the dimensionless figure of merit $ZT = \sigma S^2 T/\kappa$, where $S$ is the Seebeck coefficient, $\sigma$ the electric conductivity, $T$ the absolute temperature and $\kappa$ the thermal conductivity. The combination of highly crystalline and strongly distorted units on atomic length-scales was suggested by Slack[1] as a pathway enabling a large electronic conductivity, $\sigma$, and a low lattice contribution to thermal conductivity, $\kappa_L$, and thus, a high $ZT$. Since then, this so-called "phonon glass electron crystal" approach has been developed towards a general strategy for enhancing $ZT$ in several classes of thermoelectric materials,[2] however the subtle effects of the interplay of ordered and disordered units on atomic scales on $\sigma$ and $\kappa$ are not well understood.

The lattice contribution to heat conduction in solids can be described by two well-established limiting theoretical pictures.[3] In crystalline materials, heat is carried by harmonic eigenmodes of the lattice, called phonons. They form an ideal gas of quasiparticles with a mean free path (MFP) limited by scattering at all kinds of local imperfections that break the translational symmetry of the lattice. In addition, anharmonic bonding can cause phonon-phonon scattering. Depending on the rate of such scattering, the phonon ensemble can be viewed as a real gas or as a liquid of interacting quasiparticles with a thermal conductivity limited by Umklapp scattering. In contrast, in strongly disordered or amorphous systems, the phonon MFP can be smaller than the phonon wavelength and, consequently, the "phonon picture" breaks down. Heat is then transported by the diffusion of atomic vibrations, and is called "phonon glass" with a low $\kappa$ in the range of 0.1–1 W $m^{-1}$ $K^{-1}$ at 300 K.[4,5]

The behavior of a "phonon glass electron crystal" (PGEC) requires a very subtle combination of crystallinity and disorder to maintain sufficient electronic mobility.[2] Recent examples of PGECs include the skutterudites, where $\kappa$ is reduced by rattling dopant atoms in cage structures. The underlying causes are considered to be the resonant scattering of phonons at local vibrations as well as scattering at induced static-distortions.[6,7] In $Zn_4Sb_3$ thermoelectric compound, disordered Zn interstitials with large anisotropic thermal displacements are considered as being the relevant scattering centers for phonons.[8] In the high-temperature thermoelectric compound $Cu_{2-x}Se$ and $SrZnSb_2$, distorted Cu layers in-between crystalline Se sites and

---

Dr. L. Wu, Q. Meng, D. Su, Q. Li, Y. Zhu
Brookhaven National Laboratory
Upton, NY 11973, USA
E-mail: zhu@bnl.gov
Prof. C. Jooss
University of Goettingen
37077 Goettingen, Germany
Prof. J.-C. Zheng
Department of Physics
Xiamen University
Xiamen 361005, China
Dr. H. Inada
Hitachi High Technology
Ibaraki 312-0032, Japan

DOI: 10.1002/adfm.201301098

planar faults of Sr layers, respectively, give rise to a remarkable decrease of lattice thermal conductivity.[9,10] Similarly, sheets of disordered atoms in the misfit layered cobaltates, such as $Na_xCoO_2$,[11] $(Ca_2CoO_3)_{0.62}CoO_2$[12] and $Bi_{2-x}Pb_xSr_2Co_2O_y$,[13] are considered to cause low in-plane thermal conductivities in the range of 1–4 W $K^{-1}$ $m^{-1}$ that are dominated by the phonon contribution.[14] A common structural feature is their electrically conducting crystalline $CoO_2$ layers with strong electronic correlations that are separated by insulating layers whose periodicity is incompatible with that of the $CoO_2$ layers. This incompatibility causes the misfitting layers to induce in their neighboring layers highly reproducible incommensurate distortions, an intrinsic deterministic disorder. Clearly, the absolute value and the temperature dependence of $\kappa(T)$ of these overall crystalline PGEC compounds rule out the overall dominance of glassy heat transport; seemingly, a combination of glassy-like and phonon-type of lattice dynamics governs the $\kappa$. The determination of the mechanisms that are in play at the border between the two limiting cases of phonon- and glassy-types of dynamics is a grand challenge. In particular, separating out the underlying types of static and dynamic atomic displacements, and identifying their specific effects on phonon and electron states, so far has been beyond the grasp of experimental and theoretical research.

An essential primary step for the identification of PGEC mechanisms is the accurate determination of type and concentration of atomic and nanoscale disorder. Here, we identify the specific role of anisotropic static- and dynamic-atomic displacements in layered cobaltate $(Ca_2CoO_3)_{0.62}CoO_2$ crystals. Among the cobaltates, $(Ca_2CoO_3)_{0.62}CoO_2$ (often approximated as $Ca_3Co_4O_9$) is of particular interest because its $ZT$ is above one at high temperature. The second step for the identification of the specific PGEC mechanisms is the calculation of phonon and electron density of states and scattering rates by ab initio calculations. However, this is tremendiously difficult for the large unit cell (108 atoms) of the superstructure involved. Accurately measuring static and dynamic atomic displacements allows us to assess the vibrational density of states based on the Debye model. Electronic density of states is determined by density functional theory (DFT) calculations.

Ab initio molecular dynamic calculations of the scattering rates involving phonons and local atomic vibrations for modeling thermal conductivity are presently out of reach. Based on approximate quantum-mechanical calculations of scattering rates, we give strong evidence that in addition to Umklapp scattering which dominates $\kappa(T)$ at high temperatures, two main mechanisms dominate $\kappa(T)$ at low and medium temperatures, respectively: low-frequency phonon modes are effectively scattered at glass-like atomic vibrations via resonance scattering, while the high-frequency phonon modes are strongly scattered at modulated atomic displacements, both occurring within the disordered $Ca_2CoO_3$ layers. Both of these effects are essential in obtaining an overall reduction of $\kappa(T)$. In contrast, metal-like properties of the electrons in the crystalline $CoO_2$ layers are well maintained by these types of anisotropic static and dynamic disorder in the $Ca_2CoO_3$ layers since DFT calculations show the emergence of an insulator-metal transition of the crystalline $CoO_2$ layers due to the effect of the disordered layers.

## 2. The Effect of Displacement on Image Intensity

The structure of the $(Ca_2CoO_3)_{0.62}CoO_2$ has been extensively studied by X-ray-, neutron-, and electron-diffraction,[15,16] spectroscopy[17,18] and first-principle calculations.[17,19] The average structure of the compound consists of two interpenetrating subsystems of a $CdI_2$-type $CoO_2$ block and a distorted triple-layered rocksalt-type $Ca_2CoO_3$ block, incommensurately parallel to the ***b***-axis. Both subsystems have common ***a***-, ***c***-axes and $\beta$-angle with $a = 0.483$ nm, $c = 1.084$ nm, and $\beta = 98.14°$. The ***b***-axis lengths are $b_1 = 0.282$ nm for the $CoO_2$ subsystem and $b_2 = 0.456$ nm for the $Ca_2CoO_3$ subsystem (Figure S1, Supporting Information).[15] Accurate determination of the local, non-periodic atomic modulations and displacement in the rocksalt subsystem is not a trivial task due to the lack of superlattice peaks in diffraction; nevertheless, it is essential for understanding the system's electrical and thermal conductivity. Here, we report a method we developed to measure local displacement in $(Ca_2CoO_3)_{0.62}CoO_2$. Unlike diffraction analysis that derives the overall displacement in the two sublattices from the intensities of Bragg reflections, we directly measure the atomic displacement in real space, thereby enabling us to refine independently the atomic displacement of the $CoO_2$ and $Ca_2CoO_3$ layers that is crucial to revealing their different nature in phonon scattering.

The experiment was carried out on the aberration-corrected scanning-transmission electron microscope (STEM), Hitachi HD2700C.[20] One advantage of the instrument is that it allows simultaneous acquisition of annular-dark-field (ADF) images with different detectors covering different scattering-angle ranges (e.g., the high-angle-ADF (HAADF), and the medium-angle-ADF (MAADF)). **Figure 1** shows the HAADF/MAADF image pairs of the incommensurate structure of $(Ca_2CoO_3)_{0.62}CoO_2$. The cations in the $CoO_2$, CoO, and CaO layers are clearly visible in both imaging modes when viewed along the [010] direction, though the contrast of the CoO layer is diffusive along the [100] direction, especially in the MAADF image. The layer intensities decrease in the order of $CoO_2$, CoO, and CaO in the HAADF image (Figure 1d), so roughly following the $Z$-contrast rule; thus, over a period of 2.275 nm along the [010] direction there are 8 Co in the $CoO_2$ layer, 5 Co in the CoO layer, and 5 Ca in the CaO layer. The MAADF image (Figure 1e), however, shows that the intensity of the atomic column of the CoO layer is higher than that of the $CoO_2$ one, i.e., a contrast reversal, suggesting that local static- and thermal-displacement may play a significant role in determining the image intensity. When viewed along the [001] direction, both the HAADF and MAADF images (Figure 1 b,c) display strong, sharp Co1 columns, while the Co2 and Ca columns are weak and diffusive, indicating a large in-plane thermal displacement in the $Ca_2CoO_3$ block.

To explain the effect of local displacement on the ADF image in $(Ca_2CoO_3)_{0.62}CoO_2$, we conducted extensive calculations using the multislice method with a frozen phonon approximation, which has been demonstrated to have excellent quantitative agreement with experiments.[21] To model the structure, we adopted a supercell containing 8-$CoO_2$ and 5-$Ca_2CoO_3$ sublattices (Figure S1, Supporting Information), based on the fundamental structure refined by Miyazaki et al.[15] Figure S2 (Supporting Information) plots the calculated intensity ratio of $I_{Co2}/I_{Co1}$ as a function of thickness and collection angle. We

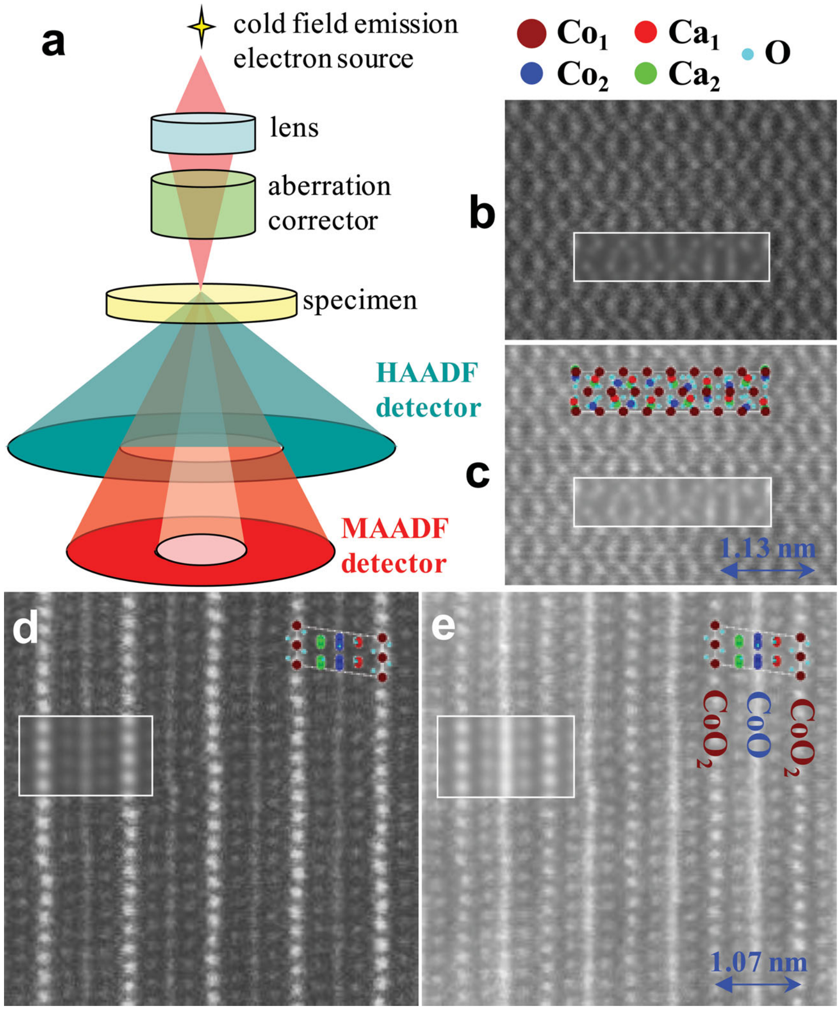

**Figure 1.** Experimental setup and observations. a) Schematic of simultaneous acquisition of HAADF and MAADF images to determine the displacive modulation in (Ca$_2$CoO$_3$)$_{0.62}$CoO$_2$. b–e) STEM images of the [001] projection (b,c) and the [010] (d,e) projection of (Ca$_2$CoO$_3$)$_{0.62}$CoO$_2$ simultaneously recorded on the HAADF and MAADF detectors with collection angle of 114–608 mrad (b,d) and 46–104 mrad (c,e). The sample thicknesses, determined by zero-loss electron energy-loss spectroscopy (EELS), were 26 nm and 35 nm for (b,c) and (d,e), respectively, and the measured spherical aberration coefficient $C_s = -75$ nm. The simulated images using the multislice calculations with the frozen phonon approximation and the refined structure are embedded in the images with a defocus $\Delta f = 0.6$ nm.

note that the intensity ratio decreases with the collection angle, but increases with the thickness; similar observations were reported for SrTiO$_3$.[20,21] Clearly, collection angle and thickness alone cannot explain the contrast reversal.

We calculated the displacement based on the cosine and sine components of the Fourier terms of the modulation waves that are commonly used for incommensurate modulation[15,16](see Supporting Information). The image intensities were then calculated by adding the displacements to the fundamental structure. In **Figure 2**a,b we plot the averaged intensities of the CoO$_2$ and CoO layers as well as their ratio $I_{\mathrm{CoO}}/I_{\mathrm{CoO2}}$ as a function of the thermal and static displacement at the CoO layer. As is evident, the effect of the displacements at the CoO layer on image intensity strongly affects the intensity of the CoO layer itself, but with little effect on its CoO$_2$ neighbors. The MAADF intensity first rises, then gradually decreases with the increase in displacement. The behavior remarkably differs from that of HAADF, and provides a unique opportunity for accurately measuring local atomic positions. We attribute the origin of the difference in the two imaging modes to dynamical diffraction near the high-symmetry crystal axes, i.e., the propagation of a focused incident electron probe in an intense narrow channeling peak centered on an atomic column that decreases and broadens when the atoms of the column become misaligned from the optical axis due to crystal tilt or strain.[22,23] Consequently, fewer electrons are scattered into the HAADF detector, but more into the MAADF detector.

Strain induced ADF contrast has been observed in various systems although no quantitative measurement has been reported.[23,24] Taking advantage of the unique sensitivity to displacement in MAADF imaging, we, for the first time, were able to directly measure local displacement through structure refinement, based on a series of HAADF and MAADF image pairs. **Figure 3**a shows an enlarged experimental image-pair of (Ca$_2$CoO$_3$)$_{0.62}$CoO$_2$. The intensity profiles obtained by averaging intensity along the [100] axis are shown in Figure 3e. Contrast reversal is clearly seen between the CoO$_2$ plane and the CoO plane in the MAADF image, indicating a much larger displacement in the latter than that in the former. Moreover, the intensity of the CaO layers across the CoO layer is not symmetric, suggestive of a larger displacement of CaO on the left side than on the right side of the CoO plane. Therefore, the space group of the supercell is better described using Cm (0 1–$p$ 0),[15] rather than C2/$m$ (0 1-$p$ 0) that would yield the same displacement for both CaO layers.[16]

## 3. Accurate Determination of Static and Thermal Displacement

We started refinement of the displacive structure based on the fundamental-, or unrelaxed-, structural model proposed by Miyazaki et al. using X-ray and neutron diffraction.[15] Compared with the experimental observations (Figure 3a), the calculated intensity of the CoO layers based on the unrelaxed structure model were too high in the HAADF image (left in Figure 3b), while too low in the MAADF image (right in Figure 3b). We then calculated both images based on the relaxed structure model refined by these authors. The agreement between the calculated images (Figure 3c) and the observations (Figure 3a) was still poor. For example, the calculated

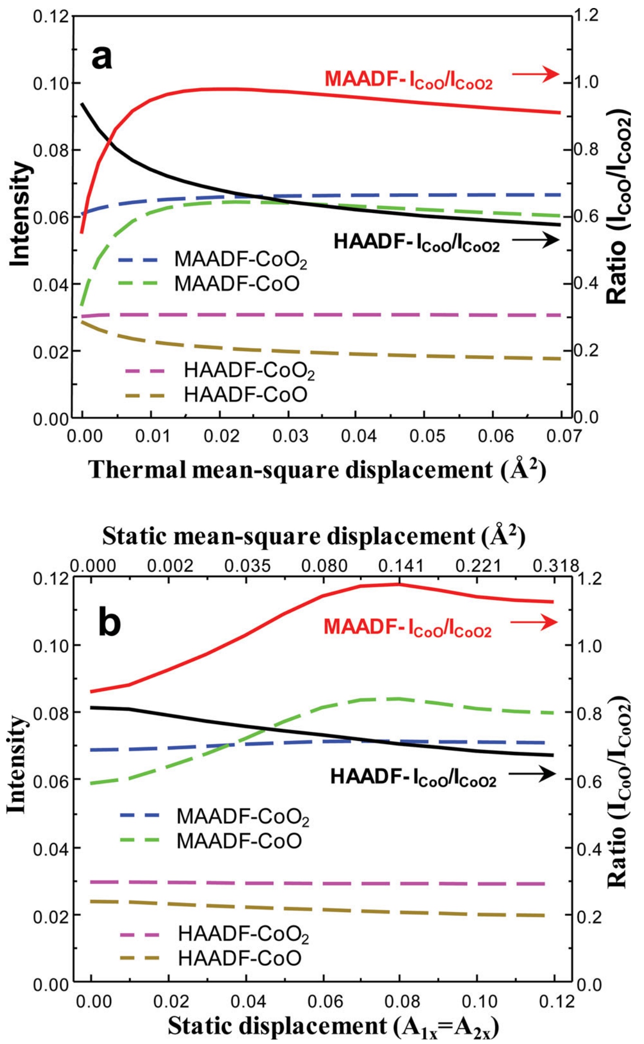

**Figure 2.** Image intensity and displacement. a,b) Calculated intensities (dashed lines) in the $CoO_2$ and CoO layers and intensity ratios $I_{CoO}/I_{CoO2}$ (solid lines) for HAADF (collection angle: 114–608 mrad) and MAADF (collection angle: 46–104 mrad) as function of a) thermal mean-square displacement in the CoO layer and b) static displacement calculated as two cosine components, $A_{1x}$ and $A_{2x}$, of the Fourier terms of the modulation waves and the equivalent mean-square static displacement in the CoO layer. The image intensities were calculated for 31.7 nm thickness and averaged over the [100] direction. We note the intensity variation due to thermal and static displacements differs significantly in MAADF. For thermal displacement, even small vibrations (0.01 A$^2$) reduce the coupling among the reflections, thus the intensity. For static displacement, in a modulated structure the displacement does not alter the crystal symmetry, thus the coupling between the reflections remains strong. In other words, the intensity does not decrease until a relative large displacement (0.14 Å$^2$) is induced, yielding contrast reversal ($I_{CoO}/I_{CoO2} > 1$) in MAADF imaging.

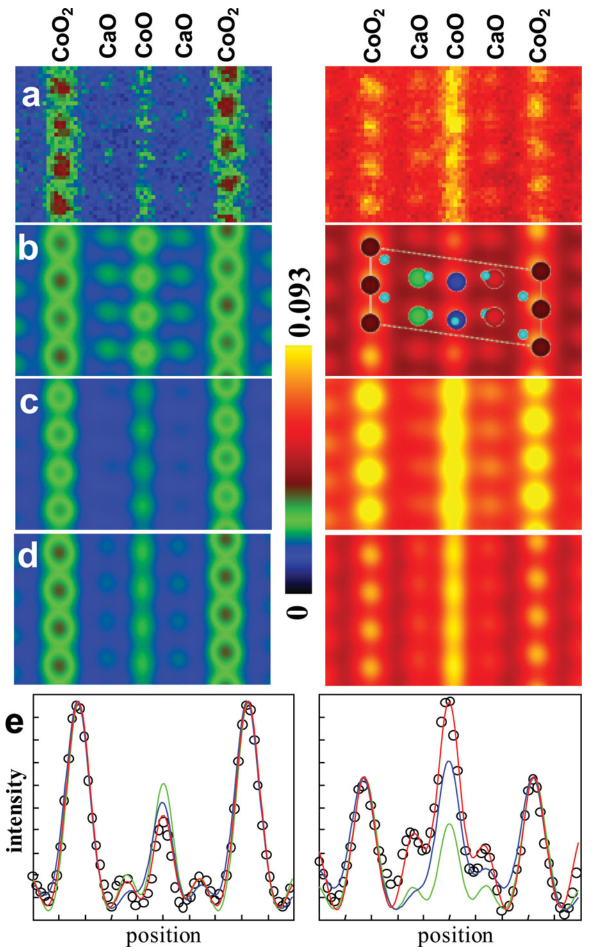

**Figure 3.** Determination of static and thermal displacement in $(Ca_2CoO_3)_{0.62}CoO_2$ single crystal. a–d) STEM images viewed along the [010] direction using the simultaneous HAADF (left panel, collection angle: 114–608 mrad) and MAADF (right panel, collection angle: 46–104 mrad) image mode. a) Experimental image. b–d) Calculated images with Miyazaki's unrelaxed model (b), Miyazaki's relaxed model (c), and our refined structure model (d). The [010] projection of Miyazaki's unrelaxed model is embedded in (b). The intensity values as color legend are shown in the middle. e) Profiles by averaging the intensities along the [100] direction (vertical direction in the figure). The open circles and green-, blue-, and red-lines are projected intensity profiles along the vertical direction normalized with the $CoO_2$ layers from (a–d), respectively. Although all the images qualitatively agree with the HAADF images (left panel), only our refined model ((d), see Table S1 in the Supporting Information) quantitatively agrees with the experimental HAADF and MAADF observations (open circles and the red lines in (e)). Area thickness is estimated to be 35 nm from EELS measurement, and finally refined to be 36.3 nm.

intensity of the $CoO_2$ layer in the HAADF was too low, while it was too high in the MAADF image; similarly, the calculated intensity of the CaO layer did not agree with the experimental observation. The poor agreement lies in the fact that Miyazaki's model has similar displacements among all atomic layers because the diffraction refinement cannot effectively distinguish the displacement in different atomic layers in the absence of superlattice reflections. Apparently, the Fourier terms of the modulation waves must be refined to fit our new experimental data that are sensitive to the displacements and resolve each atomic layer in the unit cell.

To quantitatively compare the image intensities of the experiment with the calculation, we use the intensity profile by averaging image intensity along the [100] direction (Figure 3e). The $\chi^2$ was then used to test the goodness of fit. The values of $\chi^2$ for the intensity profile calculated from Miyazaki's unrelaxed model were 2.23 for HAADF, and 4.74 for MAADF. It was slightly improved to 2.01 for HAADF, and 3.59 for MAADF, for Miyazaki's relaxed model. Extended calculations made by systematically changing the parameters reveal that, to achieve a good fit, the static- and thermal-displacements must be very small in all directions for the $CoO_2$ subsystem, and in the ***c*** direction for the $Ca_2CoO_3$ subsystem. However, large static- and thermal-displacements in the ***a***- and ***b*** directions for the $Ca_2CoO_3$ subsystem are required to fit the experimental HAADF- and MAADF-image pairs. Combined with image pairs in other orientations (Figure 1b,c), we ascertained those local atomic displacements crucial to the system's thermoelectric properties. Table S1 (Supporting Information) lists the refined Fourier amplitudes of the fractional coordinates and thermal parameters. The $\chi^2$ for our refined model were much smaller, 0.87 for HAADF, and 0.95 for MAADF suggesting a significant improvement over Miyazaki et al.'s refinement from X-ray and neutron diffraction.

Our refined structure reveals that both static and thermal displacements are mainly confined within the $Ca_2CoO_3$ block, especially in the CoO layer. The large static displacement therein strongly affects the channeling peaks when viewed along the [010] modulation direction, resulting in low HAADF but high MAADF intensities. In contrast, in the other projection, e.g., [001], the large thermal displacements in the block significantly reduce the channeling peaks, so engendering weak and diffusive contrast in both imaging modes. Clearly, this distinctive behavior is invaluable in quantitatively unfolding static disorder and local thermal lattice vibrations (see Supporting Information for quantification).

## 4. The Effect of Displacement on Phonon Scattering

Separating out quantitatively the subtle effects of static and thermal disorder, respectively, in the rigid crystalline $CoO_2$, and the soft and disordered $Ca_2CoO_3$ sublayers is the first and essential prerequisite for elucidating the microscopic origin of the lattice's low thermal conductivity $\kappa$ (**Figure 4**, for details see Supporting Information). The electronic thermal conductivity was not considered here because it is much smaller than, only about 1% of, the lattice thermal conductivity based on our experiment,[25] as well as based on the Wiedemann-Franz law.[14] Secondly, the vibrational and phonon density of states (DOS) of both sublayers has to be determined. Since the mean square displacements are rather strong (of the order of 0.06–0.15 Å$^2$ static and 0.03–0.04 Å$^2$ thermal), and the high frequency atomic scale vibrations in the THz range entirely dominate the DOS, we selected the Debye model for the direct calculation of the DOS from the measured thermal displacements (Figure S3, Supporting Information). To analyze phonon-scattering mechanisms, we started with Umklapp- and Rayleigh-scattering both of which are the well-established main scattering mechanisms for single crystals. The resulting frequency-dependent phonons mean free path (MFP) can be described with only two free parameters, *A* and *B*, that respectively reflect the crystal's anharmonicity, and the concentration of point scatters. The fit of $\kappa(T)$ in Figure 4a is very good for the simple cubic oxide MgO single crystal (the blue line) that we chose as our reference system,[26] but was very poor for $(Ca_2CoO_3)_{0.62}CoO_2$ (red line),[14] especially at temperatures below 70 K.

To reconcile this discordance, we directly determined, from the refined structure, the scattering rates of two additional scattering mechanisms, modulation-induced displacement, and resonance scattering. The resulting frequency-dependent MFP from displacement scattering is calculated from the refined atomic displacements via quantum-mechanical scattering theory. Notably, the frequency dependence of displacement scattering is similar to Rayleigh scattering (Figure 4b). Rayleigh-like scattering cannot only be ascribed to the interaction of phonons with point-like defects, but has been also attributed to local fluctuations in density or force constants, such as those observed in amorphous systems.[27] Without considering displacement scattering, the contribution of Rayleigh scattering due to point defects would be more than four orders-of-magnitude too strong in comparison with MgO. This would require there being extensive numbers of point defects in the sample that was not experimentally observed. Resonance scattering happens if propagating phonons with angular frequency $\omega$ are in resonance with a band of more or less localized modes at $\omega_0 \pm \Delta\omega_0$ in the soft disordered layer created by the vibrations of the $CoO_2$- and $Ca_2CoO_3$-subunits. Such a band of more or less localized in-plane vibrations of $CoO_2$- and $Ca_2CoO_3$-subunits with soft bonding is directly visible in the 5–10 THz range of the DOS in Figure S2 (Supporting Information). The frequency-dependent MFP is determined via a coupled harmonic oscillator model. The resulting fit of the thermal conductivity along the ***b***-direction ($\kappa_b$) of the misfit layered $(Ca_2CoO_3)_{0.62}CoO_2$ is depicted by a black line in Figure 4a. Umklapp- and Rayleigh-scattering have been kept as background effects that are present in all materials, but only slightly modify the fitting for the cobaltates.

Using modulation-induced displacement and resonance scattering as determined without any free parameter from the structure, the fitting of $\kappa(T)$ is reasonably good; Figure 4c shows the contribution of the individual scattering mechanisms to it. A schematic drawing on displacement and resonance scattering is included in Figure 4d,e. We are fully aware that it might be possibly to obtain fits of $k(T)$ with similar "goodness" based on other hypothetical scattering models and using various free parameters. However, we want to emphasize that in our approach we have only left one free parameter for Umklapp scattering. All other scattering parameters as well as the vibrational density of state are determined by experiment with the highest possible accuracy. Furthermore, displacement, resonance- and Umklapp-scattering contribute differently to the total $\kappa(T)$ in different temperature regimes. At low temperatures, the available low-frequency phonon modes with $\omega$ below a few THz are effectively scattered by resonance scattering, and dominate $\kappa(T)$. At intermediate temperatures between 80 K and 300 K, higher frequency modes of phonons of $\omega$ of several 10 THz become thermally excited and are effectively scattered at modulated atomic displacements. In this intermediate temperature-range, $\kappa$ is mainly limited by displacement scattering. With further increasing temperature, the enhanced phonon density reflects the rising contribution of Umklapp scattering. Consequently $\kappa(T)$ starts to decline as temperature rises above

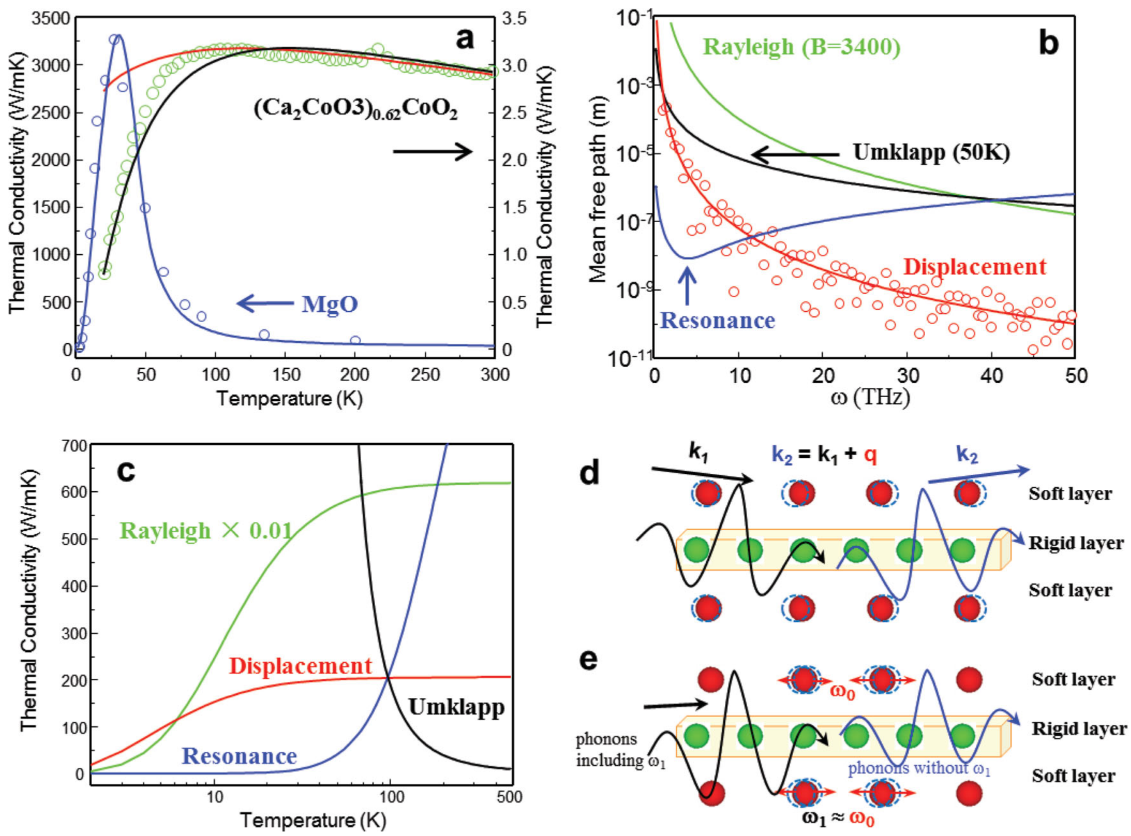

**Figure 4.** Mechanisms of thermal conductivity in the layered cobaltate compared to simple cubic MgO. a) Thermal conductivity $\kappa$ vs. temperature. Circles are experimental data for $(Ca_2CoO_3)_{0.62}CoO_2$ along the $b$ direction (green, right vertical axis) and MgO (blue, left vertical axis) taken from ref. [13,24], respectively. Solid lines are fitting curves based on specific heat, DOS, group velocity, and MFP. The blue and red lines are the fitting curves only containing the Umklapp and Rayleigh terms, while the black line including the additional displacement and resonance terms for $(Ca_2CoO_3)_{0.62}CoO_2$. b) MFP for Umklapp scattering at 50 K (black); Rayleigh scattering calculated with coefficient $B = 3400$ (green); modulation-induced displacement scattering (open circles); and resonance scattering (blue). The frequency dependent MFP of the displacement scattering is discrete because of discrete Fourier components of the displacements. A fitting curve based on the empirical $\omega^{-4}$ relation for displacement scattering is shown with the red line. c) Individual contributions from different scattering mechanisms on thermal conductivity as a function of temperature. For comparison the scale for Rayleigh scattering is reduced by a factor of 100. d,e) Schematics of displacement scattering (d) and resonance scattering (e). Green and red balls represent atoms in the rigid and soft layers, respectively. Atoms in the soft layer (red balls) deviate from its periodical positions (dashed circles) in (d) due to the displacement, resulting in phonon scattering. $\boldsymbol{k}^1$ and $\boldsymbol{k}^2$ are exemplarily represented wave vectors of the incident and scattered phonons, and $\boldsymbol{q}$ is the Fourier component of the displacement. Dashed circles in (e) represent local vibration of the atoms. If phonons (black curve) with frequency of $\omega_1$ tune into resonance with a local vibration at $\omega_0$ ($\omega_1 \approx \omega_0$), they can be absorbed. Phonons outside of the resonance frequency band will propagate.

$T = 150$ K. Even in the high-temperature branch above 300 K (see Figure S4 of the supplemental material), the extrapolation of the fitting of $\kappa(T)$, which was done for $T < 300$ K, well describes the experimental data. Thus, the high temperature $\kappa$-regime of the misfit layered $(Ca_2CoO_3)_{0.62}CoO_2$ compound is controlled by Umklapp scattering and the obtained value for the Umklapp coefficient is well validated.

## 5. The Effect of Displacement on Electronic Structure

In previous sections and the supplemental materials, we present detailed information about the rigid frame of the $CoO_2$ layers, and the significant displacive modulation in the $Ca_2CoO_3$ layers, and then discuss the effects of such displacements on the lattice thermal conductivity. In this section, we consider first-principles calculations based on density functional theory (DFT) to elucidate the band structure of $(Ca_2CoO_3)_{0.62}CoO_2$. In particular, we analyze the displacive-modulation-induced local electronic properties in the $Ca_2CoO_3$ layers, and the effect of the distorted $Ca_2CoO_3$ layer on the density of states of the $CoO_2$ layer to gain an understanding of the "electron crystal"-like electric-transport behavior.

One finding from our general gradient approximation (GGA+U) calculations is that the electronic properties of $(Ca_2CoO_3)_{0.62}CoO_2$ are very sensitive to the local structure of the $Ca_2CoO_3$ and $CoO_2$ layers. Detailed analysis of the band structure indicates remarkable differences in the electronic states of the square $Ca_2CoO_3$- and the triangular-$CoO_2$ sublattices. The stacking of the two layers with different electric conductivity creates the pronounced anisotropy of the electronic transport.

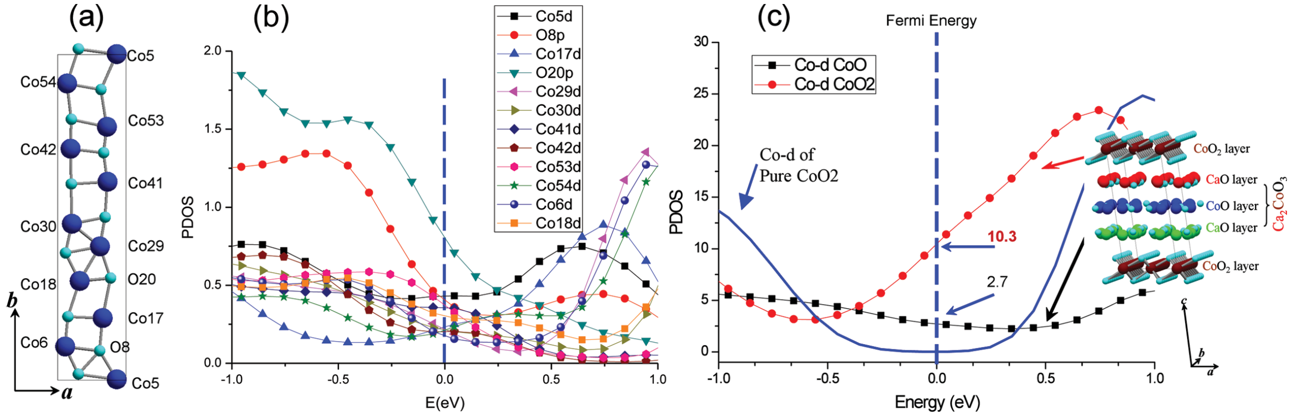

**Figure 5.** Density functional theories calculations using GGA+U for the partially disordered $(Ca_2CoO_3)_{0.62}CoO_2$. a) Displacive modulation of the CoO layer in the $Ca_2CoO_3$ subsystem. b) The projected density of states (pDOS) of d-states of each Co (labeled in (a) in the CoO layer). The Fermi energy is marked by the dashed line. c) The total pDOS of Co d-states of the CoO layer and the $CoO_2$ layer with the structural unit shown on the right. In addition, the pDOS of the infinite layer compound $CoO_2$ is shown and represents a Mott insulator. Note the total pDOS of Co d-orbital in the ordered $CoO_2$ layer (red symbol-line) is three times more than that of Co d-orbital in the disordered CoO layer (black symbol-line) at the Fermi level.

In particular, for the $Ca_2CoO_3$ layer, the local electronic structure is strongly tied to atomic displacements (**Figure** 5a,b). Several Co-ions in the $Ca_2CoO_3$ layer exhibit a large projected density-of-states (pDOS) at Fermi level, while most have rather small pDOS due to distorted structural features (Figure 5a). We also notice that the pDOS of O atoms in the CoO layers shows large fluctuation (Figure 5b), suggesting the sensitivity of the electronic structure of O to local atomic environment, while that in the $CoO_2$ layer are almost identical (not shown). This observation confirms that the electrical conductivity mainly comes from the $CoO_2$ layer in $(Ca_2CoO_3)_{0.62}CoO_2$.

Figure 5c compares the total pDOS of Co d-orbital of the infinite layer $CoO_2$ parent compound with that of the crystalline $CoO_2$ layer in $Ca_3Co_4O_9$ and that of the disordered CoO layer. Our GGA+U study reveals that the infinite layer $CoO_2$ parent compound is a Mott insulator. In contrast, the $CoO_2$ layer which is embedded by the distorted $Ca_2CoO_3$ shows a metal-like density of states near the Fermi level (the total pDOS of Co d-orbital in $CoO_2$ layer is three times more than that in the CoO layer). Carefully examining the pDOS of Co d-orbital contribution of CoO layer reveals that the metallic band in CoO layer is more localized than that in $CoO_2$, thus reducing the overall electric conductivity of the CoO layer. Our calculations thus provide detailed insights into the origin of "electron-crystal" characteristics of a partially disordered system, namely, they reflect disorder-induced localization of d-orbital in the CoO layers, and an ordered structure and larger pDOS at Fermi energy in the $CoO_2$ layer.

Our spin-polarized DFT calculations further illustrate that different spin states of Co exist in the CoO and the $CoO_2$ layers. We obtained a total magnetic moment of $41.3\mu_B$ per unit cell in the ferromagnetic (FM) state, or absolute magnetic moment of $35.6\mu_B$ per unit cell in the antiferromagnetic (AFM) state. This corresponds to about $1.6\mu_B$ per Co atom for the FM state, or $1.4\mu_B$ per Co atom for the AFM state, larger than the reported value of $1.09\mu_B$ per Co atom,[19] but agreeing well with the experimental value of $1.3\mu_B$ per Co atom for $T <$ 400 K.[12] The reason why our calculations differ from previous calculations and agree better with experimental measurements can be attributed to the fact that the atomic structures used for the calculations are different. In our current calculations, presented herein, we use the refined structure which has a supercell containing 108 atoms, while a simplified 42-atom-DFT-relaxed supercell was employed in previous calculations.[19] We noted that the DFT relaxation by atomic force is sensitive to the size of the $Ca_3Co_4O_9$ supercell. Although the DFT relaxed structure using 108-atoms is more close to the refined structure than that using 42-atoms, it has smaller displacements in the $Ca_2CoO_3$ sublayer in comparson with the experimentally refined structure.

A difficult question for magnetic measurement is which Co atoms, in the CoO or $CoO_2$ layers, are responsible for the observed magnetic moment. Based on our spin-polarized DFT calculations, we find that the value of the magnetic moment of Co in the CoO layers is $\approx 2.3–2.5\mu_B$ per Co, while it is only about $0.2\mu_B$ per Co in the $CoO_2$ layers, pointing to the strong magnetic anisotropy of cobaltate.

## 6. Discussion

Our detailed experimental and theoretical study of the atomic-, electron- and phonon- structure of the misfit cobaltate gives new insights into the fundamental mechanisms of the high thermoelectric performance of the material. The major advantage of the real-space measurement of the displacement is that both thermal and static displacement in the $CoO_2$ and $Ca_2CoO_3$ layers can be measured and refined separately; this cannot be done using the reciprocal space or diffraction method. Particularly, the real-space measurement supports a clear analysis of the distribution of disordered and ordered crystallographic regions with subatomic accuracy. Strong atomic displacements are only present within the $Ca_2CoO_3$ layer and not within the $CoO_2$ layer, in contrast to other reports based on reciprocal space methods, but in agreement with a recent STEM study published by Klie at al.[28]

The ability to distinguish between static and dynamic displacements is crucial for determining the effect of disorder on phonon- and electron-properties. As demonstrated in Figure 2, the dependence of the MAADF image intensity on thermal and static displacements differs significantly when viewed along the direction of modulation. This feature allows us to separate one from the other. As revealed from our quantitative analysis, electron channeling occurs along the aligned atom columns in a low-index crystal orientation. The channeling effect decreases the intensity of HAADF images, but increases that of the MAADF images in the presence of misaligned atoms from the optical axis caused by local disorder. A further increase in displacement reduces dynamic coupling among the reflections, eventually lowering the intensity of the MAADF images. The position of the maximum MAADF intensity strongly depends on the nature, static or thermal, of the displacement. Static modulation displacement preserves the superlattice symmetry and, thus, the coherence of the reflections, yielding strong dynamic coupling even at large displacements (Figure 2b). For thermal vibration, the high-energy imaging electrons in the microscope traveling at about the half speed of light, take only a fraction of femtosecond to pass through the sample that is much faster than the speed of the atomic thermal oscillation. Therefore, the imaging electrons see that the atoms in the sample deviate from their equilibrium positions in a stationary configuration with a broken crystal symmetry due to random thermal displacement, thereby reducing dynamic coupling, even at a small mean-square value (0.01 $A^2$, i.e., one order-of-magnitude less than that of static displacement, Figure 2). When viewed along non-modulation directions, static displacement shifts the atomic positions in the ADF images, but has little effect on image contrast, while thermal displacement decreases the contrast, but does not alter atomic positions.

The identification of the specific relations between static- and dynamic disorder and phonon scattering mechanism in the misfit cobaltate is challenging and would require the application of ab initio molecular dynamic methods to extremely large supercells. In order to shed light on the mechanisms that play at the border of phonon and glassy dynamics, and thus, on the origin of phonon glass electron crystal (PGEC) behavior in layered disordered systems, we used the refined static and dynamic disorder as a starting point for quantum mechanical perturbation theory. Although the acentrosymmetric static displacements within the $Ca_2CoO_3$ layer create a strong scattering potential for phonons they enhance anharmonicity because the potential energy is not a harmonic function of the displacement. Even though a perturbation calculation may be only a rough approximation due to the strong static and dynamic displacements, our calculations yield a reasonable agreement between measured and calculation $\kappa(T)$ using only one free parameter for Umklapp scattering. In particular, we find strong evidence that resonance scattering can effectively suppress low-frequency acoustic phonons modes because of the large in-plane vibrations of the soft $Ca_2CoO_3$ layer with respect to the rigid $CoO_2$ layer. The presence of resonance scattering is supported by two observations: i) These "soft local vibrations" are directly revealed by our scattering method and constitute a high DOS at relatively low frequency (Figure S3, Supporting Information). ii) Resonance scattering can easily explain the suppression of the low-temperature branch of $\kappa(T)$ because it provides an efficient mechanisms for scattering the low-frequency phonon excitations that propagate in-plane within the crystalline $CoO_2$ layer. In contrast, the high-frequency modes of the crystalline $CoO_2$ layer can be easily scattered by displacement and Umklapp scattering.

An important feature of a PGEC system must be a deterministic process of disorder generation that entails a well-reproducible type and amplitude of atomic displacements. Indeed, in the misfit layered cobaltates, the interaction between the incommensurate sublayers provide a mechanism for deterministic generation of displacements. This is shown by our additional DFT GGA+U calculations using the ideal CaO+CoO layers without $CoO_2$, revealing, in the CaO+CoO system, that the optimized structure is always relaxed to the perfect rock-salt structure. This indirectly supports our conclusion in previous section that there is strong electronic interaction between $CoO_2$ and $Ca_2CoO_3$ layers. The existence of the $CoO_2$ layers drives the large distortion of CaO and CoO in $Ca_2CoO_3$. If the interaction between $CoO_2$ and $Ca_2CoO_3$ layers is weak, for example, close to the van der Waals limit, then the $Ca_2CoO_3$ layer will not be distorted as strongly as observed experimentally. This result contrasts with the claim in ref. [28] that the bonding between the $CoO_2$ and the $Ca_2CoO_3$ layer is weak. Moreover, the $CoO_2$-$Ca_2CoO_3$-interaction-induced distortion destroys the spin and orbital ordering in the $Ca_2CoO_3$ layer, resulting in some locally metallic-like DOS in the band structure. For the ideal rock-salt CaO+CoO structure, our calculations of the AFM state demonstrate its insulating nature, similar to that in pure AFM-CoO. For the parent compound of triangular cobaltates, $CoO_2$, our DFT+U calculations show that it is a Mott insulator, consistent with previous calculations.[29] Note that experiments find a bad metal, which may be close to a Mott transition[30] and properties that may sensitivly depend on sample purity and residual dopands. Indeed, we find that the electronic properties of $CoO_2$ layers are quite sensitive to doping and bonding. The large difference between Co d- states in the pure $CoO_2$ compound and those in $CoO_2$ layer of $(Ca_2CoO_3)_{0.62}CoO_2$ (Figure 5c), points to an insulator-metal transition due to a major influence of $Ca_2CoO_3$ layer on the electronic properties of the $CoO_2$ layer. This confirms our finding that there is a strong electronic interaction between the $CoO_2$ and $Ca_2CoO_3$ layers.

## 7. Conclusions

Combing the refined structure of $(Ca_2CoO_3)_{0.62}CoO_2$, including accurately measured static and thermal lattice disorder, with phonon scattering and DFT calculations, we derived two major conclusions on the atomistic mechanisms underlying its large thermoelectric power. First, the interaction between two incommensurate crystalline layers generates a partially disordered crystal, wherein the anisotropic static and dynamic displacements are almost entirely localized in the $Ca_2CoO_3$ sublayer. This preserves high electric conductivity within the crystalline $CoO_2$ layer, whereas the disordered $Ca_2CoO_3$ layer does not contribute significantly to electric conductivity. Our findings offers insight into the atomic mechanisms of the "phonon glass" (CoO) and "electron crystal" ($CoO_2$) of the system. Second, among various possible mechanisms for reducing thermal conductivity in layered systems, we identified phonon scattering due to large in-plane atomic displacement in the $Ca_2CoO_3$ block, and resonance scattering due to large in-plane vibrations between the two sublayers that cause a reduction in $\kappa$ over a wide temperature range. Therefore, these scattering mechanisms represent an efficient means for reducing out-of-plane- and in-plane-thermal conductivity, and are the underlying mechanisms for considering the layered misfit compound as an approximant of the "phonon glass–electron crystal" concept. Our refined structure may initiate future work on the origin of the large Seebeck coefficient that may be associated with the degenerated configuration of different valence states, or the spin states of Co atoms in the crystalline $CoO_2$ layer induced by its interaction with the disordered $Ca_2CoO_3$ layer.[12,31]

## 8. Experimental Section

*Experimental Methods*: Single $(Ca_2CoO_3)_{0.62}CoO_2$ crystals were prepared using the flux method as described in ref. [32]. The STEM samples were carefully prepared using an ion mill at low voltages. The STEM-ADF images were taken with the aberration-corrected Hitachi HD2700C STEM, equipped with five electron- detectors, including the HAADF and MAADF ones. The image signals from both detectors were simultaneously recorded to ensure the image pairs had the same imaging conditions but different collection angles (convergent angle of 27 mrad, and collection angles of 114–608 mrad for HAADF and 46–104 mrad for MAADF were used in the present study). The probe function of the electron beam was measured using CEOS software with gold particles deposited on a carbon film. The STEM image calculations were carried out with our own computer codes running on GPU (Nvidia GeForce 590, 1024 cuda cores) based on the multislice method with a frozen phonon approximation.[21,33] The calculated STEM images were convoluted with a 0.15 nm FWHM Gaussian spread function to compare with the experiment.

*Calculations of Vibrational and Phonon Density of States*: The vibrational and phonon density of states of $(Ca_2CoO_3)_{0.62}CoO_2$ were calculated using the Debye model. The total MFP was calculated based on Callaway's treatment of the Peierls-Boltzmann phonon-gas theory. The coefficients of Umklapp and Rayleigh scattering used in the calculations were obtained by fitting the calculations with the measured thermal conductivities of $(Ca_2CoO_3)_{0.62}CoO_2$ and MgO.

*Calculations of Electronic Structure*: The DFT calculations were carried out using the pseudopotential plane-wave method with general gradient approximation (GGA). To test our results, we also performed the full potential calculations using the LAPW method. It is noted that the band structure and magnetic moments of Co predicted by the two methods are similar. It is well known that in rocksalt CoO, the strongly correlated effects play an important role in determining its band structure. The GGA+U method was used to investigate the strong correlation effect in Co d-orbitals. An effective $U = 4$ eV was chosen, which is the same as that for Co in $Na_xCoO_2$.

## Supporting Information

Supporting Information is available from the Wiley Online Library or from the author.

## Acknowledgements

The authors would like to thank P. B. Allen for his stimulating discussions on phonon scattering and thermal conductivity. Work at Brookhaven, including the use of Center for Functional Nanomaterials, was supported by the U.S. Department of Energy, Office of Basic Energy Science, Material Science and Engineering Division, under Contract No. DE-AC02-98CH10886 and the work of C.J. was supported by DFG SPP 1386. J.C.Z. was supported by SRFDP No. 20090121120028.

Received: March 29, 2013

[1] G. A. Slack, *CRC Handbook of Thermoelectrics*, CRC Press, New York **1995**, p. 407.
[2] G. J. Snyder, E. S. Toberer, *Nat. Mater.* **2008**, *7*, 105.
[3] D. G. Cahill, R. O. Pohl, *Ann. Rev. Phys. Chem.* **1988**, *39*, 93.
[4] D. G. Cahill, S. K. Watson, R. O. Pohl, *Phys. Rev. B* **1992**, *46*, 6131.
[5] P. B. Allen, J. L. Feldman, *Phys. Rev. Lett.* **1989**, *62*, 645.
[6] G. S. Nolas, D. T. Morelli, T. M. Tritt, *Ann. Rev. Mater. Sci.* **1999**, *29*, 89.
[7] B. C. Sales, *Int. J. Appl. Ceram. Technol.* **2007**, *4*, 291.
[8] G. J. Snyder, M. Christensen, E. Nishibori, T. Caillat, B. B. Iversen, *Nat. Mater.* **2004**, *3*, 458.
[9] B. Yu, W. Liu, S. Chen, H. Wang, H. Wang, G. Chen, Z. Ren, *Nano Energy* **2012**, *1*, 472.
[10] Ø. Prytz, E. Flage-Larsen, E. S. Toberer, G. J. Snyder, J. Taftø, *J. Appl. Phys.* **2011**, *109*, 043509.
[11] M. Lee, L. Viciu, L. Li, Y. Wang, M. L. Foo, S. Watauchi, P. A. Pascal Jr, R. J. Cava, *Nat. Mater.* **2006**, *5*, 537.
[12] A. C. Masset, C. Michel, A. Maignan, M. Hervieu, O. Toulemonde, F. Studer, B. Raveau, J. Hejtmanek, *Phys. Rev. B* **2000**, *62*, 166.
[13] I. Terasaki, H. Tanaka, A. Satake, S. Okada, T. Fujii, *Phys. Rev. B* **2004**, *70*, 214106.
[14] A. Satake, H. Tanaka, T. Ohkawa, T. Fujii, I. Terasaki, *J. Appl. Phys.* **2004**, *96*, 931.
[15] Y. Miyazaki, M. Onoda, T. Oku, M. Kikuchi, Y. Ishii, Y. Ono, Y. Morii, T. Kajitani, *J. Phys. Soc. Jpn.* **2002**, *71*, 491.
[16] D. Grebille, S. Lambert, F. Bouree, V. Petricek, *J. Appl. Cryst.* **2004**, *37*, 823.
[17] T. A. Tyson, Z. Chen, Q. Jie, Q. Li, J. J. Tu, *Phys. Rev. B* **2009**, *79*, 024109.
[18] G. Yang, Q. Ramasse, R. F. Klie, *Phys. Rev. B* **2008**, *78*, 153109.
[19] R. Asahi, J. Sugiyama, T. Tani, *Phys. Rev. B* **2002**, *66*, 155103.
[20] H. Inada, L. J. Wu, J. Wall, D. Su, Y. Zhu, *J. Electron Microsc.* **2009**, *58*, 111.
[21] J. M. LeBeau, S. D. Findlay, L. J. Allen, S. Stemmer, *Phys. Rev. Lett.* **2008**, *100*, 206101.
[22] R. F. Loane, E. J. Kirkland, J. Silcox, *Acta Cryst.* **1988**, *A44*, 912.
[23] Z. H. Yu, D. A. Muller, J. Silcox, *J. Appl. Phys.* **2004**, *95*, 3362.
[24] J. L. Lee, J. Silcox, *Ultramicroscopy* **2000**, *84*, 65.
[25] Q. Li, unpublished.
[26] G. A. Slack, *Phys. Rev.* **1962**, *126*, 427.
[27] J. E. Graebner, B. Golding L. C. Allen, *Phys. Rev. B* **1986**, *34*, 5696.
[28] R. F. Klie, Q. Qiao, T. Paulauskas, Q. Ramasse, M. P. Oxley, J. C. Idrobo, *Phys. Rev. B* **2012**, *85*, 054106.
[29] P. H. Zhang, W. D. Luo, V. H. Crespi, M. L. Cohen, S. G. Louie, *Phys. Rev. B* **2004**, *70*, 085108.
[30] C. de Vaulx, M.-H. Julien, C. Berthier, S. He´bert, V. Pralong, A. Maignan, *Phys. Rev. Lett.* **2007**, 98, 246402.
[31] W. Koshibae, K. Tsutsui, S. Maekawa, *Phys. Rev. B* **2000**, *62*, 6869.
[32] J. Sugiyama, C. T. Xia, T. Tani, *Phys. Rev. B* **2003**, *67*, 104410.
[33] E. J. Kirkland, *Advanced Computing in Electron Microscopy*, Plenum Press, New York **1998**.